41st AIAA Fluid Dynamics Conference and Exhibit
27 - 30 June 2011, Honolulu, Hawaii

AIAA 2011-3584

Non-Reacting and Reacting Flow in a Swirl-Stabilized Burner for Ultra-Wet Combustion

Steffen Terhaar*, Katharina Göckeler*, Sebastian Schimek*,
Sebastian Göke*, and Christian Oliver Paschereit†
Chair of Fluid Dynamics, Technical University of Berlin, D-10623, Germany

The flow field of a swirl-stabilized burner for ultra-wet combustion is experimentally investigated by assessing the isothermal and the reacting flow. The ultra-wet combustion technique promises high cycle efficiency and low NO_x emissions. Investigations of the non-reacting flow field are carried out in a water tunnel facility and the reacting flow is assessed in an atmospheric combustion test rig. Experiments were conducted at a theoretical swirl number of 0.7 and Reynolds numbers in the range of 22,000 to 32,000. Particle Image Velocimetry and OH*-Chemiluminescence are employed to measure the flow velocities as well as the spatial distribution of heat release. The effect of steam addition up to levels of 30% of the air mass flow is investigated for natural gas fuel and mixtures of natural gas and hydrogen. The results show a strong impact of steam addition on the flow field and the position of the reaction zone. In particular, three different flow patterns were found. Dry flames and hydrogen flames show a broad inner recirculation zone with very low local turbulent kinetic energy. At high rates of steam dilution, the flow fields show good agreement to the non-reacting flow field in water as well as in isothermal air. At intermediate to high steam dilution rates the flame shows a trumpet like shape. Several sudden changes of the flow field and flame shapes could be observed for various operating conditions.

Nomenclature

$\dot{m}$	Mass flow
$\dot{V}$	Volume flow
d	Diameter of the combustion chamber
D_h	Hydraulic diameter of burner outlet
I	Abel deconvoluted OH*-chemiluminescence intensity
I^*	Normalized Abel deconvoluted OH*-chemiluminescence intensity
I_t	Turbulence intensity
L_t	Integral length scale
r	Radial position
r_p	Radial position of the peak axial velocity
$R_{u'}$	Spatial correlation function
Re	Reynolds number
S	Swirl number
T_{ad}	Adiabatic flame temperature
T_{in}	Inlet temperature of air, steam and fuel mixture
u	Mean axial velocity
$u'_{\mathrm{rms,fl}}$	Root mean square of the axial velocity in the reaction zone
u_0	Bulk velocity at burner outlet
u_{fl}	Mean axial velocity in the reaction zone
V	Volume
v	Mean radial velocity
$w_{\mathrm{H_2}}$	Mass fraction of hydrogen in the fuel
x	Axial position
x_{fl}	Axial position of the center of gravity of the reaction zone
x_m	Axial length of the measurement plane

Symbols

α	Initial opening angle of the emanating jet
Ω	Degree of humidity
ϕ	Equivalence ratio

*PhD student, Chair of Fluid Dynamics, Hermann-Föttinger Institut, Technische Universität Berlin, Müller-Breslau-Str. 8.
†Professor, Chair of Fluid Dynamics, Hermann-Föttinger Institut, Technische Universität Berlin, Müller-Breslau-Str. 8.

I. Introduction

Using the exhaust heat for steam generation in humidified gas turbines (HGT) promises high cycle efficiencies at low NO_x emissions. Compared to combined cycle power generation, humidified cycle gas turbines have the advantage that no steam turbine is required, which reduces plant complexity and installation costs. Furthermore, steam can effectively be used for cooling of turbine blades and hot combustor parts. A review of different humidified gas turbine cycles is provided by Bartlett and Westermark,[1,2] and Jonsson and Yan.[3]

The presence of steam influences the combustion process resulting in lower NO_x emissions in two important manners. The reduced flame temperature constrains the production of thermal NO_x. Additionally, steam alters the concentration of active species, influencing the NO_x formation pathways.[4,5] Therefore, even at constant adiabatic flame temperatures, NO_x is reduced with increasing humidity. This allows for higher equivalence ratios, which are favorable in terms of process efficiency.

One challenge of ultra-wet combustion of natural gas is the decreased flame stability at high steam dilution rates due to the reduced reaction rate and flame temperature. However, the reduced reactivity with steam decreases the risk of flame flashback when operating with hydrogen fuel. Hence, steam addition allows for the combustion of hydrogen-rich fuels and hydrogen at low NO_x emissions.[6]

Swirl-stabilized combustors are widely used in gas turbines to enhance mixing, reduce pollutants and improve flammability limits. The swirling flow expands at the burner exit due to circumferential forces, leading to radial pressure gradients coupled with an adverse axial pressure gradient along the centerline. If the swirl intensity is sufficient, a stagnation point, followed by a recirculation zone, is formed in the center. The deceleration of the flow, the continuous upstream transport of hot combustion products and the increased turbulence improve the flame stabilization.[7]

In 1963, Clarke et al.[8] carried out flow visualization experiments in a swirl-stabilized confined combustor using water, isothermal air and a reacting air-propane mixture. They found that the velocity fields (i.e. the flow pattern) were very similar for all cases though small changes due to density effects occurred.

Chigier and Dvorak[9] investigated in 1974 the effect of combustion on a weakly swirling jet without confinement and concluded that chemical reaction and temperature changes caused only minor variations to the main flow field at swirl numbers less than $S = 0.3$.

In contrast, in 1981, Fuji and Eguchi[10] used Laser Doppler Anemometry (LDA) to measure the effect of combustion on a strongly swirling jet without confinement. They compared measured velocity and turbulence profiles and observed a much shorter but wider recirculation zone in the reacting case. The absolute turbulent kinetic energy was found to be increased by combustion. Though, due to the increased velocity, the turbulent kinetic energy, normalized by the local maximum axial velocity, is decreased.

More recently, Wicksall et al.[11] measured the flow field in a swirl-stabilized combustor with confinement using Particle Image Velocimetry (PIV). They compared the velocities in a 30 mm x 30 mm region near the burner outlet for isothermal air, methane combustion and hydrogen enriched methane combustion. Their findings were that combustion, as well as the fuel composition, have an impact on the flow field. However, the size of the recirculation zone was found to be not significantly affected by combustion, which was attributed to the confinement of the burner.

Vanoverberghe et al.[12] carried out a parametric study with a similar swirl-stabilized combustor as in the current study and identified various flame configurations. Transitions of the flame states were found to depend on the equivalence ratio, swirl number and the degree of fuel-air unmixedness. The terms V-shaped and M-shaped flame, which will be used in the current study, were used by Durox et al.[13] to distinguish laminar flames that spread from a central flame stabilizer, showing a V-shape, or from both the central flame stabilizer and the edge of the burner, showing an M-shape.

The effect of dilution, though not necessarily steam dilution, on flame properties of a reactive mixture has been studied extensively. Three basic mechanisms[14] are known: (a) the concentration of reactants in the reactive mixture is reduced; (b) the flame temperature is reduced due to absorption by the diluent of parts of the heat released by the reaction; (c) the additive may alter reaction paths, producing a chemical effect.

Recently, Mazas et al.[14] investigated the laminar flame speed of methane flames with increasing steam contents. Their findings were that the laminar flame speeds decrease quasi linearly with increasing steam molar fraction, even at high steam dilution rates.

Not much research has been done regarding the influence of steam on the flow field and the flame configurations in a swirl-stabilized combustor. In the scope of the GREENEST project Göke et al.[6] used OH* chemiluminescence to identify the spatial resolution of heat release. Steam addition resulted in a less defined flame anchoring more downstream in the combustor. Krüger et al.[15] had similar findings conducting

a Large Eddy Simulation (LES) with a reduced reaction mechanism. The simulation also yielded significant changes in the reacting flow field due to steam addition.

Gu et al.[16] investigated an air-propane flame behind a bluff body under dry and moderately humid conditions. They observed a smaller recirculation zone in the humid case and a decreased partially-quenching limit, which they explained by the increased chemical reaction time of the humid air flame.

To the author's knowledge no detailed studies about the influence of steam dilution on the flow field in a swirl-stabilized combustor have been published. Knowledge of the flow field will improve the understanding of the effect of steam addition, help to achieve enhanced flame stabilization at high steam levels and provide information for accurate modeling of the combustion.

The remainder of this study is structured as follows: (1) the experimental approach and the investigated configuration will be explained; (2) the isothermal flow fields of water and air are compared; (3) the results of the reacting flow will be presented, discussed, and compared to the isothermal flow; (4) conclusions of steam dilution as well as of hydrogen addition to the fuel are drawn.

II. Experimental Approach

The generic burner used in this study is shown in Figure 1(a). Air and steam are premixed before entering the burner at the swirl generator, where angular momentum is imparted to the flow. Fuel is injected directly downstream of the swirl generator through 16 holes arranged in a circle in the bottom plate of the burner. The swirling flow mixes with the fuel in the annular passage to the combustion chamber.

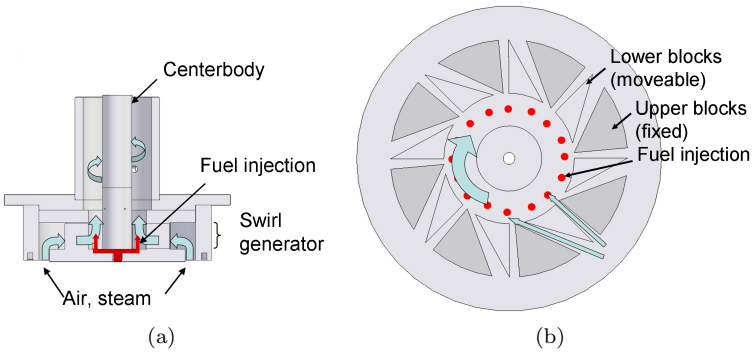

Figure 1. Generic burner (a) and movable block swirl generator (b).

The swirl generator is based on the movable block principle with variable radial and tangential passages as sketched in Figure 1(b). The measurements of the current study were carried out at a fixed swirl number of $S = 0.7$.

A 300 mm long silica glass tube with a diameter of 200 mm was used as the combustion chamber. At the end of the exhaust tube an end orifice with a contraction ratio of 11:1 was applied to suppress possible thermoacoustic instabilities.

Gas-fired tests were conducted in an atmospheric test rig. The air was preheated and perfectly mixed with overheated steam upstream of the generic burner. The steam content Ω was defined as the ratio of the mass flow rate of steam $\dot{m}_{\text{steam}}$ to the mass flow rate of air $\dot{m}_{\text{air}}$:

$$\Omega = \frac{\dot{m}_{\text{steam}}}{\dot{m}_{\text{air}}}. \tag{1}$$

While the steam content was varied between Ω =0 to 0.3, the mass flow of air plus steam was kept constant at $\dot{m}_{\text{air+steam}}$=180 kg/h. Hydrogen addition to the natural gas fuel is defined by the mass fraction of hydrogen.

$$w_{H_2} = \frac{\dot{m}_{H_2}}{\dot{m}_{CH_4}} \tag{2}$$

Cold flow experiments were carried out in a vertically oriented water tunnel. The test section has a square cross-section consisting of four glass windows, providing full optical access to the mounted combustor model.

Measurements of combustor velocity fields in water tunnels are commonly used due to the relative simplicity of measurements because of lower flow velocities at similar Reynolds numbers and excellent seeding quality for optical measurement techniques. Hence, data for a wide range of geometrical and inlet parameters are usually available or can be easily obtained. Furthermore, water tunnel measurements can be excellently combined with mixing experiments assessing for instance the fuel-air unmixedness for premixed or partially premixed flames.

A detailed descriptions of the water tunnel and combustion test facilities can be found in recent publications from Göckeler et al.[17] and Göke et al.,[5] respectively.

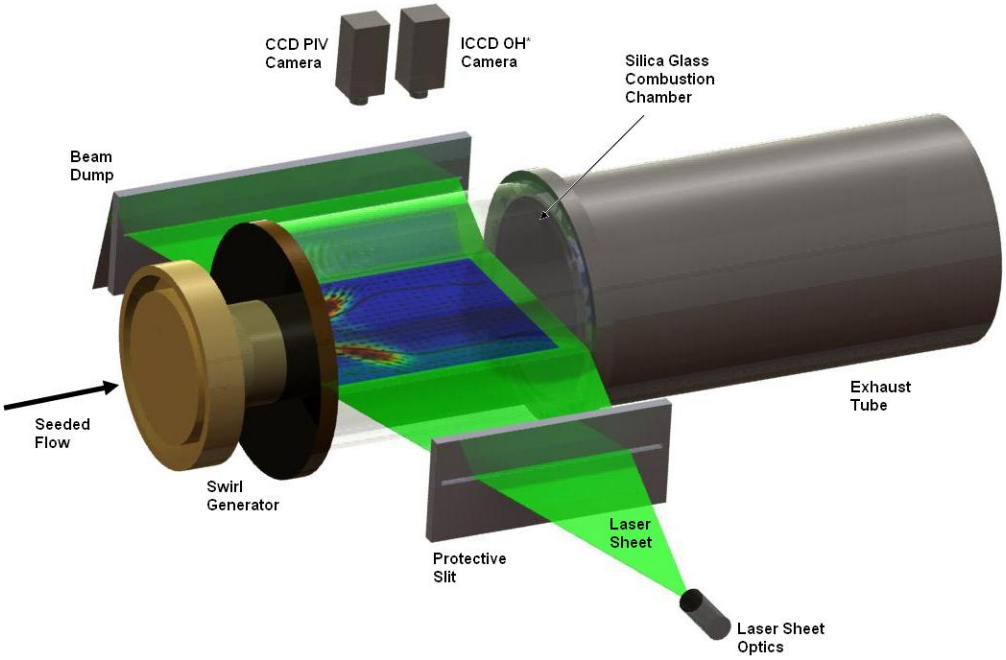

Figure 2. Sketch of the experimental setup in the combustion test rig.

Figure 2 shows a sketch of the experimental setup for the velocity measurements in the combustion chamber. Flow velocities were measured using Particle Image Velocimetry (PIV) at a horizontal plane containing the combustor axis. For the measurements of the reacting flow in the combustion test rig a 150 mJ per pulse Nd:YAG laser and a 2048 px x 2048 px CCD camera recording at a frequency of 7 Hz were used. The laser sheet had a width of 260 mm and a thickness of 1 mm. The time delay between the pulses was set according to the expected flow velocities between 6 and 12 μs. The strong out-of-plane velocity component associated with swirling flows required a rather short pulse separation in order to minimize lost particle pairs. Aluminum oxide particles of a nominal diameter of 1 μm were seeded into the flow upstream of the swirl generator using a fluidized bed seeding generator. Reflections of the incoming laser light at the silica glass were minimized by using beam dumps for the sheet and primary reflections. Further reflections could be eliminated by sandblasting parts of the silica glass. However, this leads to increased background light. Only approximately 50 to 100 pictures could be taken in one measurement since residuals of seeding particles quickly deteriorated the image quality. Furthermore, the steam lead to corrosion of the glass, requiring regular substitution of the silica glass after less than 20 measurements.

For water tunnel measurements with the same burner geometry and at similar Reynolds numbers, the laser sheet was generated using an Nd:YAG laser (20 mJ per pulse) and 400 picture pairs (1024 px x 1024 px) per measurement were recorded by a CCD camera at a frequency of 4 Hz. Silver-coated, hollow, glass spheres with a nominal diameter of 15 μm were used as seeding particles.

The images of the water tunnel measurements and the reacting measurements were processed with a final interrogation size of 16 px x 16 px and 32 px x 32 px, respectively. The interrogation window overlap was set to 50%, resulting in a resolution of 1.3 mm and 1.6 mm, respectively. The data was filtered for outliers and interpolated from adjacent interrogation areas.

An intensified CCD camera with a bandpass filter at 308 nm was used to give the spatial distribution of

OH*-chemiluminescence, which correlates with the heat release and the intensity of the chemical reaction.

Table 1 gives an overview of the tested conditions for the isothermal measurements, the dry and wet measurements, and the measurements with a mixture of natural gas (NG) and hydrogen as fuel.

Table 1. Operating conditions of the tested cases.

Name	$\frac{T_{\text{in}}}{^\circ\text{C}}$	$\frac{T_{\text{ad}}}{^\circ\text{C}}$	w_{H_2}	ϕ	Ω	Re	$\frac{\text{Power}}{\text{kW}}$
Isoth. Water	-	-	-	-	-	26,500	-
Isoth. Air	-	-	-	-	-	38,500	-
NG Dry	180-350	1580-1900	0	0.6-0.8	0	22,500-26,000	80-108
NG Wet	185-390	1430-1580	0.1-0.3	0.7-0.9	0.1-0.3	24,000-32,000	70-98
NG-hydr. Dry	190-225	1580	0	0.6	0	27,500-29,000	84-88
NG-hydr. Wet	270-300	1580	0.1-0.2	0.8	0.1-0.2	27,000-28,000	93-98

III. Results

A. Isothermal Flow

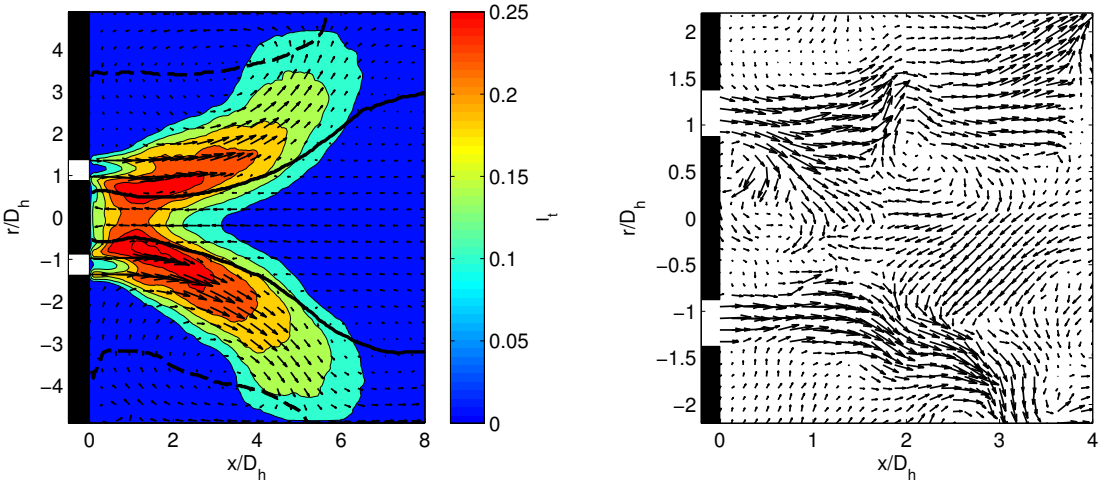

(a) Mean flow field and turbulence intensity. Solid and dashed lines indicate the borders of the reversed flow in the IRZ and ERZ, respectively.

(b) Close up near the burner outlet of an instantaneous velocity field.

Figure 3. Isothermal flow field measured in the water tunnel.

The isothermal flow field downstream of the burner is typical for swirl stabilized burners. As shown for a water tunnel measurement in Fig. 3(a), three[a] regions can be identified: an annular jet emanating from the mixing tube, an internal recirculation zone (IRZ) generated by vortex breakdown and an external recirculation zone (ERZ) induced by the area change and the confinement. In between the regions, turbulent shear layers are produced, with very high levels of turbulence. Especially in the inner shear layer turbulence levels are very high due to large scale vortices, which can be linked to convective flow instabilities triggered by a Precessing Vortex Core (PVC).[18,19] Figure 3(b) shows a close up view on the instantaneous flow field containing vortices that are convected downstream.

Figure 4 shows the axial velocity u normalized with the bulk velocity at the burner inlet u_0 and the turbulence intensity $I_t = \sqrt{0.5 \cdot \left(u'^2_{\text{rms}} + v'^2_{\text{rms}}\right)}/u_0$ for isothermal air with and without a mounted end orifice with a 11:1 contraction ratio and isothermal water flow without end orifice. At the latest axial

[a] A comparably small centerbody wake can also be identified when plotting the vectors at a higher resolution

position of $x/D_h = 9$ no data for the water flow are available.

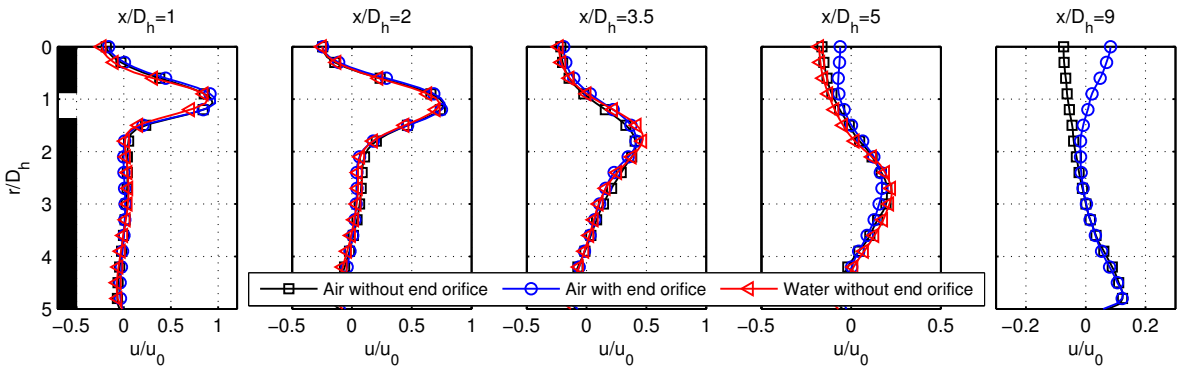

(a) Normalized axial velocity of isothermal air and water.

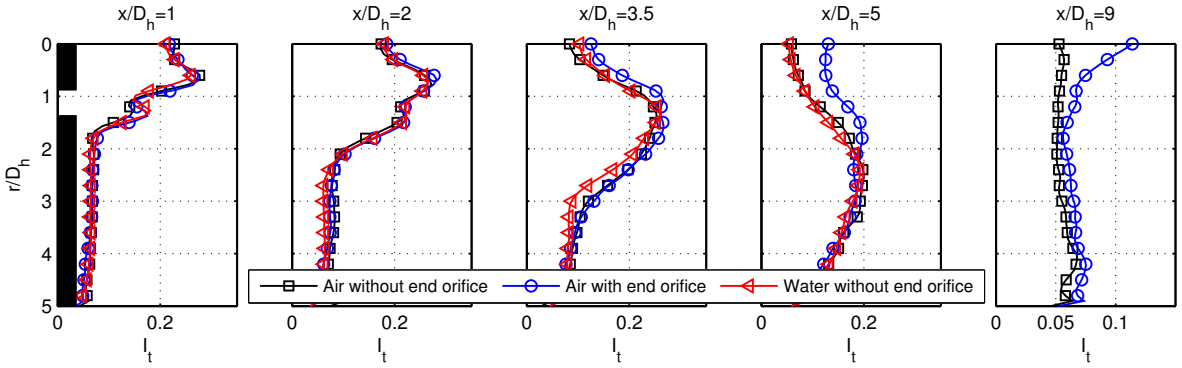

(b) Turbulence intensity of isothermal air and water.

Figure 4. Normalized axial velocity and turbulence intensity for water flow and isothermal air. Note, symbols are set to distinguish the profiles. They do not indicate the spatial resolution of the data.

It can be observed that all configurations show similar flow velocities near the burner outlet. The peaks of the axial velocity move outwards with increasing axial positions. Simultaneously, the zone of negative axial velocities gets wider. Higher velocities near the center line than for the other cases were measured at axial positions of $x/D_h > 5$ for isothermal air with mounted end orifice.

The turbulence intensity near the burner outlet shows two distinguishable peaks located in the inner and outer shear layers of the emanating jet. The peak located in the outer shear layer smears out at axial positions $x/D_h > 3.5$. Similar to the discrepancy in the axial velocity the turbulence intensity curve for the air case with mounted end orifice differs at axial positions $x/D_h > 5$. The turbulence intensity near the center line reaches up to twice the value of the case of air without end orifice.

The velocity and turbulence distribution plots indicate that the isothermal air without end orifice is in a very good agreement with the water flow case. The effect of the end orifice on the flow field can be explained by the subcritical nature of the isothermal swirling flow , where flow perturbations have a large upstream effect.[20] With combustion, swirling flows usually recover to the supercritical state[20] without a significant influence of the end orifice on the flow field. Hence, the isothermal flow without end orifice will be used in the remainder of this study for comparison purpose to the reacting flow even though an end orifice is mounted to suppress possible thermoacoustic instabilities.

B. Reacting Flow - Flame shapes

Velocity fields and OH*-chemiluminescence of the reacting flow were measured for a wide range of equivalence ratios, steam contents, fuel compositions and inlet temperatures. To classify the flames and flow fields a set of parameters was used and will be presented in the following.

The flow field near the burner outlet is described by the initial opening angle α of the emanating jet.

With the radial position of the peak axial velocity $r_p(x)$ the local opening angle $\alpha_x(x)$ can be determined.

$$\alpha_x(x) = \text{atan}\left(\frac{dr_p}{dx}\right) \tag{3}$$

The initial opening angle α is then defined as the average of α_x from x/D_h=0.5 to 4.

To asses the axial position of the reaction zone, the axial center of gravity x_{fl} of the Abel deconvoluted OH*-chemiluminescence image is defined as follows:

$$x_{\text{fl}} = \frac{\int I(x,r)x dV}{\int dV} \tag{4}$$

where $I(x,r)$ denotes the Abel deconvoluted OH*-chemiluminescent intensity distribution. Axial symmetry of the OH*-intensity is assumed.

In order to weight averaged values of the flow field with the corresponding OH*-chemiluminescence intensity the normalized intensity distribution $I^*(x,r)$ is required.

$$I^*(x,r) = \frac{I(x,r)}{\int I(x,r) dV} \tag{5}$$

Subsequently, the weighted mean axial velocity u_{fl} and the weighted averaged rms axial velocity $u'_{\text{rms,fl}}$ at the flame position defined by $I^*(x,r)$ can be calculated as:

$$u_{\text{fl}} = \int u(x,r) \cdot I^*(x,r) dV \tag{6}$$

$$u'_{\text{rms,fl}} = \int u_{rms}(x,r) \cdot I^*(x,r) dV. \tag{7}$$

Care has to be taken not to confuse the global velocity u_{fl} with the local turbulent flame speed. The actual flame itself is very thin and tends to stabilize in regions with low velocities. However, trends can be derived also from u_{fl}.

The volumes of reversed flow in the IRZ and ERZ play important roles for reactor modeling of the combustion process and can be derived from the flow field data. Since, the IRZ is not fully closed in the measurement plane, their sizes are normalized by the volume V_m corresponding to the measurement plane of the axial length x_m.

$$V_m = \pi \frac{d^2}{4} \cdot x_m \tag{8}$$

Figure 5 shows the size of the IRZ and the initial opening angle of the jet over axial position of the center of gravity of the flame for the measured cases. In Fig. 5(a) distinct regions can be found with significantly differing opening angles for flames at varying axial positions. Flames near the burner outlet show large opening angles while flames located further downstream have significantly smaller opening angles. An additional region with a very narrow opening angle can be found around x_{fl}/D_h=6 to 7. Similar regions can be found as well in Fig. 5(b) concerning the size of the IRZ. The flame shapes associated to the regions and named after their appearance are the M-shaped flames anchored very close to the burner outlet, the V-shaped flames with the CoG of the reaction zone in a region from x_{fl}/D_h=3 to 6, trumpet like flames with a very small opening angle, and the annular flames located more downstream in the combustion chamber.

The distinction of the M-shaped from the V-shaped flame, which is not very clear from Fig. 5 alone, becomes more obvious when looking at the shape of the flames in Fig. 6.

For simplification purpose 6 cases are chosen that represent the encountered flame shapes. Since the V-shaped and the annular flame cover a very wide range of axial positions of x_{fl}, a short and a long example are selected for these flame shapes. Fig. 6 shows the flow field superimposed on the spatial distribution of the Abel deconvoluted OH*-chemiluminescence intensity. The operating conditions and flow field parameters of the exemplary chosen cases are supplied in table 2.

The most compact flame was observed for mixtures of hydrogen and natural gas. This flame type is called M-flame since the reaction anchors both in the inner and outer shear layer of the emanating jet featuring an M-like shape (I). For dry, premixed, natural gas combustion the flame usually featured a V-shape (II) with the main reaction zone located only in the inner shear layer. If the steam content was increased or the

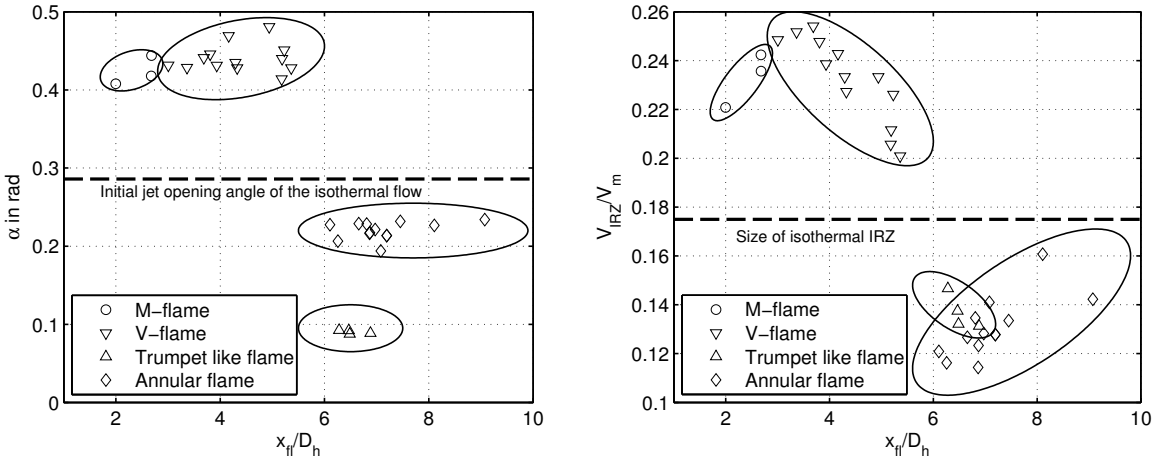

(a) Initial opening angle of the emanating jet for different axial positions of the center of gravity of the flame.

(b) Normalized size of the IRZ for different axial positions of the center of gravity of the flame.

Figure 5. Parameters of the encountered flame and flow field shapes.

Table 2. Parameters of the cases showing the encountered flame shapes.

No.	Shape	$\frac{T_{in}}{^\circ C}$	$\frac{T_{ad}}{^\circ C}$	w_{H_2}	ϕ	Ω	$\frac{x_{fl}}{D_h}$	$\frac{V_{IRZ}}{V_m}$	$\frac{V_{ERZ}}{V_m}$	$\frac{u_{fl}}{[m/s]}$	α
-	non-reacting	-	-	-	-	-	-	0.177	0.214	-	0.285
I	M	188	1580	0.2	0.6	0	2.00	0.222	0.210	41.6	0.408
II	V (short)	350	1720	0	0.65	0	3.68	0.258	0.164	25.28	0.440
III	V (long)	150	1580	0	0.8	0.1	5.17	0.209	0.243	11.01	0.417
IV	Trumpet-like	350	1580	0	0.8	0.2	6.88	0.134	0.377	13.11	0.087
V	Annular	185	1530	0	0.85	0.3	6.86	0.116	0.324	5.81	0.218
VI	Annular (long)	200	1460	0	0.9	0.3	9.07	0.144	0.269	1.35	0.234

equivalence ratio decreased the flame got longer and moved further downstream (III). At a certain degree of steam content (usually $\Omega = 0.2$) multiple stable flame positions existed. The flame either remained at a V-shape (III), showed a trumpet like form (IV) near the burner axis, or moved further downstream and showed an annular form (V). These three configurations exhibit significantly different flow field shapes and no intermediate configurations could be found. Further increase of the steam content lead to a less defined shape of the flame anchoring more downstream (VI).

The following list summarizes the operating parameters where the flame shapes could be determined. Note that for a single configuration two or even three shapes could be observed with the flame jumping suddenly from one state to another.

1. M-shaped flame (I)
   - Flames of hydrogen-natural gas mixtures (w_{H_2} =0.1 to 0.2) without steam dilution show an M-shaped flame. For w_{H_2} =0.2 and Ω =0.1 the flames moves to a very short V-shape, that can be hardly distinguished from the M-shape.
2. V-shaped flame (II-III)
   - Flames of hydrogen-natural gas mixtures (w_{H_2} =0.1 to 0.2) at high steam levels ($\Omega = 0.2$) show a short V-shape. Though higher steam levels (i.e. $\Omega = 0.3$) have not been tested, it is very likely that these flame also feature a V-shape.
   - All measured natural gas flames without steam addition. The length of the flame strongly depended on the equivalence ratio and the air inlet temperature T_{in}.

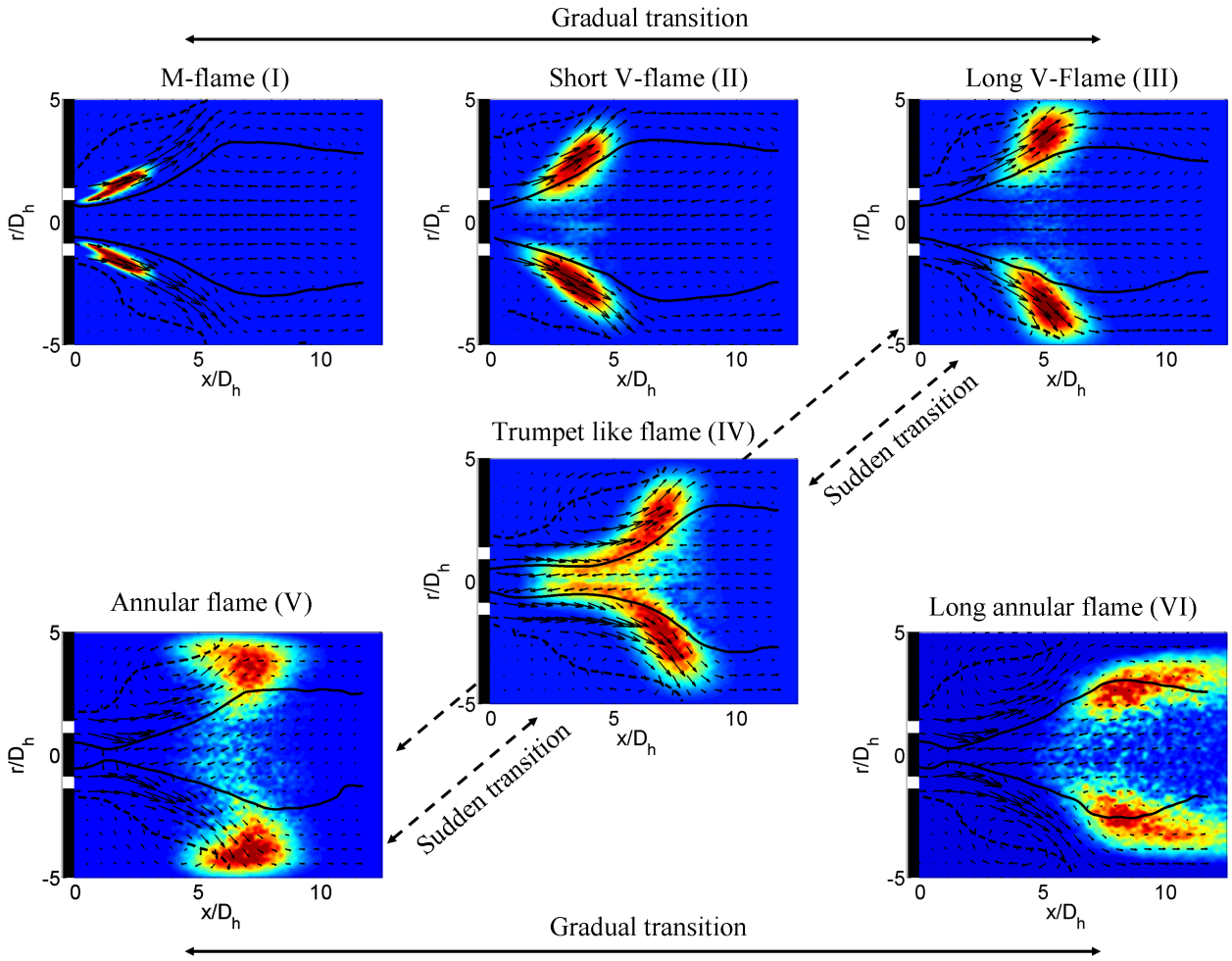

Figure 6. Overview of the encountered flame shapes for combustion of natural gas and mixtures of hydrogen and natural gas with increasing steam dilution rates. The averaged velocity field is superimposed on the averaged Abel deconvoluted OH*-chemiluminescence image. Solid and dashed lines indicate the borders of the reversed flow in the IRZ and ERZ, respectively. For operating parameters see table 2.

- Natural gas flames with low steam contents ($\Omega = 0.1$) without hydrogen addition. These flames are very susceptible to the transition to other flame shapes, in particular, trumpet shaped flames.

3. Trumpet-shaped flame (IV)
   - Natural gas flames at low and intermediate steam levels ($\Omega = 0.1$ to 0.2). At $\Omega = 0.1$ a transition to a V-shaped flame is likely, while at $\Omega = 0.2$ annular flames were often found at the same operating parameters.
4. Annular flame (V-VI)
   - Wet natural gas flames at high steam contents ($\Omega = 0.2$ to 0.3). Higher steam ratios and lower inlet temperatures lead to longer annular flames with the center of gravity of the reaction zone further downstream.
   - Wet natural gas flames at low steam contents ($\Omega = 0.1$) and low inlet air temperatures $T_{in} <$ 180°C.

Profiles of the axial velocity and the turbulence intensity are shown in Fig. 7 for the exemplary chosen flames and flow fields (table 2) at various axial positions for the encountered flame shapes (I-VI). For the purpose of comparison, profiles of the isothermal air flow are repeated. The profiles and the flame position will be described first for the M and V-shaped flames and subsequently for the trumpet like and annular flames.

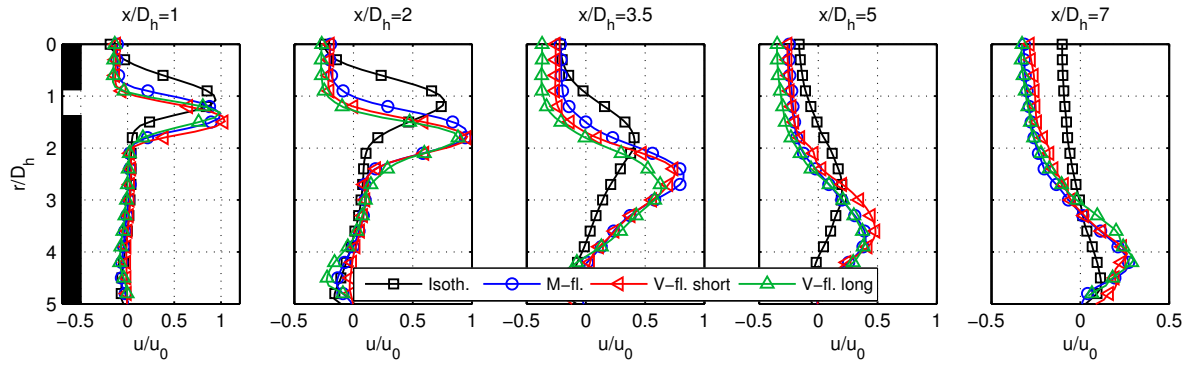

(a) Normalized axial velocity of the M-shaped and V-shaped flames.

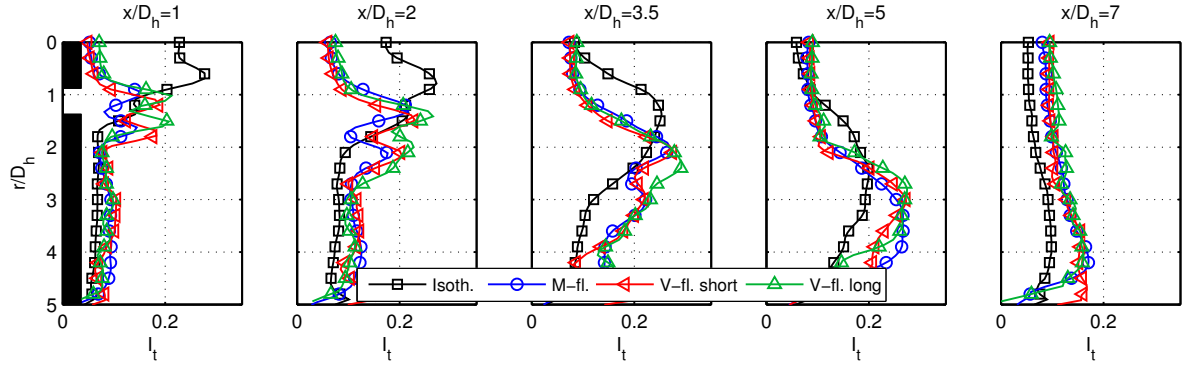

(b) Turbulence intensity of the M-shaped and V-shaped flames.

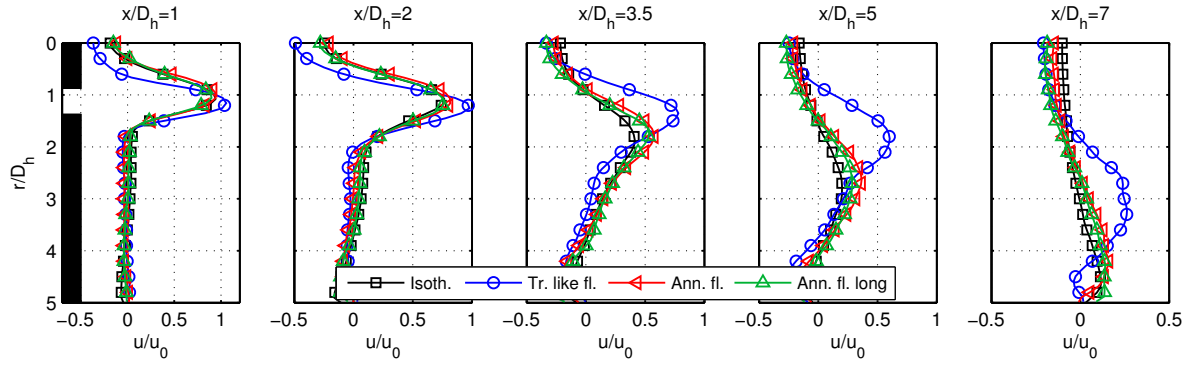

(c) Normalized axial velocity of the annular and trumpet like flames.

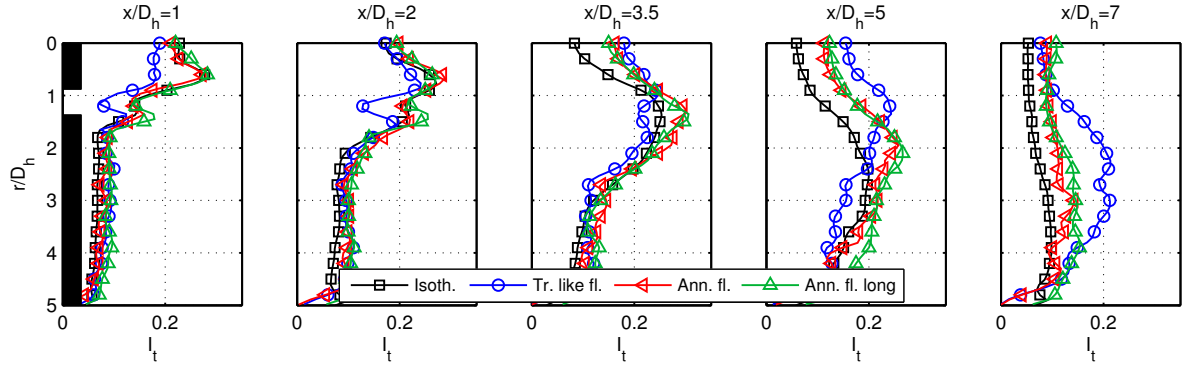

(d) Turbulence intensity of the annular and trumpet like flames.

Figure 7. Normalized axial velocity and turbulence intensity for different flame shapes.

- The M-shaped as well as the V-shaped flame (Fig. 7(a,b)) show similar normalized flow velocities near the burner outlet. Compared to the isothermal flow field significant differences can be found. The peak of the axial velocity is more outwards already near the burner outlet. This leads to to a wider IRZ. The flow velocities in the IRZ zone are almost uniform and the turbulence intensity in the IRZ near the burner outlet is significantly lower compared to the isothermal case. Similar velocity profiles were found by Vanoverberghe et al.[12] for swirl stabilized flames. Differences between the flow fields can be observed, as the peak of the axial velocity is slightly closer to the center for the M-flame resulting in a narrower IRZ near the burner outlet. This effect has already been observed by Wicksall et al.[11] Further downstream the diameter of the IRZ increases faster for the M-flame than for the long V-flame, resulting in a bigger total IRZ volume.
  Due to the high burning velocity caused by the added hydrogen, the M-flame is capable of anchoring as well in the inner as in the outer shear layer of the emanating jet near the burner outlet where the flow velocities are extremely high and turbulence intensity is low compared to the mean velocities. The V-shaped flames anchor further downstream and only in the inner shear layer.
- The trumpet like flame, appearing at intermediate to high steam contents ($\Omega = 0.1$ to $\Omega = 0.2$), exhibits a significantly different flow field than the M or V-shaped flames. The inner recirculation is extremely narrow up to axial positions of $x/D_h = 5$ where the size of the IRZ rapidly increases, though not recovering the total size of the IRZ in the isothermal flow. The plots in Fig. 7(c,d) show that the maximum negative axial velocity on the center line of the IRZ is considerably higher near the burner outlet than for the isothermal and all other reacting cases, indicating a higher recirculation than the extremely narrow IRZ would suggest.
  The trumpet like flame is located along the inner shear layer over a wide range of axial positions and follows the shape of the emanating jet.
- The annular flames, usually present at ultra-wet conditions ($\Omega = 0.2$ to $\Omega = 0.3$), exhibit similar flow fields as the isothermal flow without end orifice. Especially near the burner outlet, upstream of $x/D_h = 2$, the velocities and the turbulence intensities are hardly altered by the heat release. Further downstream, mean flow velocities are higher because of the lower density due to heat release. The turbulence intensity scales similar to the flow velocity. The shape of the velocity profile, however, remains similar with the peak of the axial velocity somewhat nearer to the center line in the reacting case. These discrepancies are of greater importance for shorter annular flames and lead to significantly decreased sizes of the IRZ at later axial positions, resulting in considerably lower measured volumes of the IRZ (see also Fig. 5(b)).
  The possible flame positions of annular flames cover a wide range of sizes and axial positions. Short annular flames are similar to long V-shaped flames and long annular flames are located further downstream and show a less defined shape.

Figures 5 and 8 show parameters defining the flame position and the flow field as a function of the the axial position of the CoG of the flame. The CoG was chosen since hereby the different flame shapes can be easily distinguished.

In Fig. 5(b) it can be observed that for all M- and V-flames the volume of reversed flow in the measured IRZ is bigger than in the isothermal case. For flames with the center of gravity of the reaction zone at an axial position around $x/D_h = 3.5$, a maximum of the IRZ size in the measured volume is obtained. A downstream movement of the flame decreases the size of the IRZ. All flames with high steam contents (trumpet like and annular flames) feature smaller sizes of the IRZ than the isothermal flow.

While for the trumpet like flame no clear trend can be found, long annular flames show a slightly increased size of the IRZ tending to the size of the isothermal flow field.

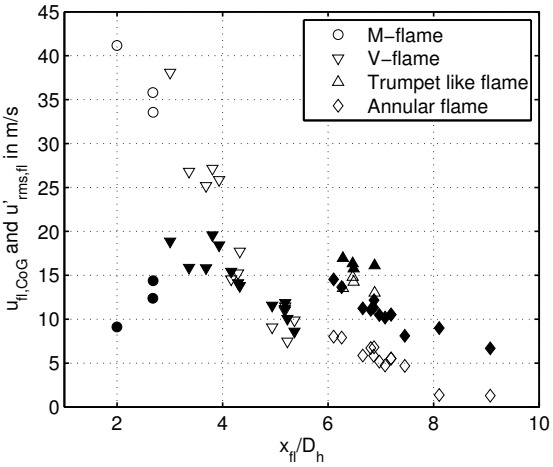

Figure 8. Mean axial flow velocity (hollow symbols) and rms velocity (filled symbols) for different axial positions of the center of gravity of the flame.

Regarding the velocities at the flame position (Fig. 8), it can be seen that for flames located near the

burner outlet the mean axial velocities at the mean position of the reaction zone are higher and turbulence is lower. For more downstream values of $x_{fl}/D_h > 4$ the velocity fluctuation are of the same magnitude as the mean velocity or even higher.

C. Transition and stabilization mechanisms

The presented results show that steam addition to the combustion process leads to 3 significantly different flame shapes and corresponding flow field shapes. The fact that the transitions from one state to another are not gradual but sudden, leads to the assumption that bifurcation points exist in the mechanisms governing the flame and flow field shapes.

Regarding the flow field in a swirl-stabilized combustors, a commonly encountered instability is the PVC. The occurrence of the PVC was shown to depend on different operating parameters, such as the equivalence ratio or the degree of premixedness. The PVC can be excited or suppressed by the heat release.[21] In the flow field of the investigated combustor this helical instability was found under non-reacting conditions in the water tunnel.[19] Oberleithner et al.[18] showed that the PVC, potentially arising from an absolute unstable flow regime, acts as the pacemaker for convective instabilities in the shear layers inducing strong vortices that entrain fluid to the jet center.

In order to gain further insight into the turbulence of the flow fields, the integral length scale of the turbulence (i.e the size of the largest energy containing eddies) at various axial positions along the center line is calculated. The integral length scale L_t is defined as the integral of the correlation function $R_{u'}(x, r, \Delta x)$:

$$R_{u'}(x, r, \Delta x) = \frac{\overline{u'(x,r)u'(x+\Delta x, y)}}{\sqrt{\overline{u(x,r)'^2}}\sqrt{\overline{u(x+\Delta x, r)'^2}}} \tag{9}$$

$$L_t(x, r) = \int_0^\infty R_{u'}(x, r, \Delta x)d\Delta x \tag{10}$$

being u' the axial velocity fluctuation, Δx the axial distance, and $\overline{(\ldots)}$ the time averaging operator.

The integral length scales in Fig.9 show similar characteristics for the annular flame and the isothermal flow. Both curves feature a zone of larger turbulence scale at the centerline near the burner outlet at axial position of $x/D_h \approx 1$. Since also the velocities and turbulence intensities of the flow field of the annular flame are very similar to the isothermal flow field, it is likely that the instability mechanisms governing the isothermal flow are also present in the flow field of the annular flame.

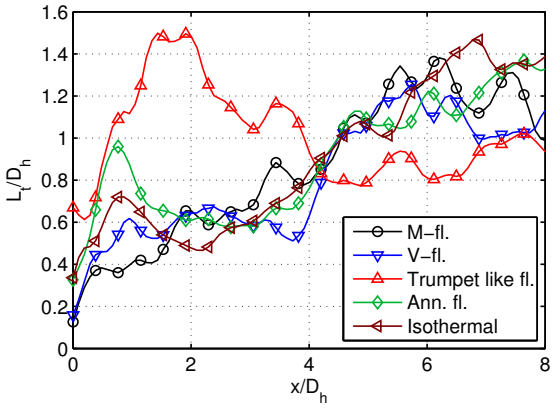

Figure 9. Integral length scale along the centerline for the encountered flame and flow field shapes.

The integral length scales for the M-shaped and V-shaped flames show different characteristics when compared to the isothermal flow. The peak at $x/D_h \approx 1$ is considerably less defined for the V-shaped flame and absent for the M-shaped flame. This indicates a change in the turbulence from the isothermal flow field to the flow field of the M and V-shaped flame. Considering the very low measured turbulence in the IRZ for the M-flame and V-flame yields the assumption that no large coherent structures are present for these flame shapes. The absence of the induced vortices combined with the higher momentum of the recirculated flow is one possible reason for the wider recirculation zone.

In contrast, Fig. 9 shows very high values of the integral length scale for the trumpet like flame at axial positions of x/D_h=1 to 4. This suggests the presence of large coherent structures in this region at the centerline. However, since the flow field differs significantly from the isothermal flow field and the integral length scale is about two times longer, it can not be assumed that the coherent structures follow the same mechanisms as in the isothermal flow field.

Transitions between the flame shapes are likely to occur due to minor stochastic perturbations. The flame stabilizes at a different position and the changes of the influence of the heat release lead to a different governing instability mechanism in the flow field (e.g. PVC). However, further investigation of the dynamical

modes of the different flame shapes is needed in order to explain the corresponding flow fields and the transition mechanisms.

IV. Conclusions

Measurements of the non-reacting and the reacting flow field in a swirl-stabilized combustor were carried out in a water tunnel and an atmospheric combustion test facility, respectively. The operating conditions covered a wide range of equivalence ratios, steam contents, inlet temperatures, and fuel compositions.

The flow fields of isothermal air and water were found to agree very well, provided that no orifice was mounted at the end of the exhaust tube. Usage of the end orifice strongly alters the flow field due to the subcritical nature of the isothermal flow field.

Three basic flame shapes and adjacent flow fields were identified using PIV and OH*-chemiluminescence measurements.

1. Dry flames and mixed natural gas-hydrogen flames with low steam dilution rates showed V-shapes or M-shaped flames, respectively. Both flow fields are similar with high negative velocities in the IRZ and a wide jet opening angle resulting in a broad IRZ. The turbulence intensity near the burner outlet is significantly reduced compared to the isothermal flow. In particular inside the IRZ very low turbulence levels were measured.

2. A trumpet like flame was found at intermediate steam levels. The flow field as well as the flame showed a particular form with a very narrow IRZ with combustion along the inner shear layer.

3. At high steam dilution rates the flames showed annular shapes located in a broad range of axial positions further downstream than for the other flame shapes. The flow fields of the annular flames showed a good agreement with the isothermal flow. The form of the velocity and turbulence profiles was hardly altered near the burner outlet. Further downstream flow velocities are higher due to heat release and the IRZ is slightly narrower. Turbulence profiles are scaled similar to the velocity profiles.

Rapid spontaneous transitions between the flame shapes and flow field shapes were found. Different hydrodynamical instability mechanisms governing the flow field were considered as possible explanations for the flow field shapes.

The axial position of the center of gravity of the Abel deconvoluted OH*-chemiluminescence intensity and the initial opening angle of the emanating jet were used to clearly identify the flame and flow field shapes. Further, it was shown that the size of the inner recirculation zone directly depends on the axial position of center of gravity of the Abel deconvoluted OH*-chemiluminescence intensity.

The good agreement between the flow field of the annular flame and the isothermal flow field of water and air (without mounted end orifice) is of great importance for the use of water tunnel testing, in order to assess easily the effects of geometrical parameters on the flow field or to carry out advanced mixing experiments, that cannot be done in the reacting flow.

Acknowledgements

The research leading to these results has received funding from the European Research Council under the ERC grant agreement n° 247322, GREENEST.

The authors would like to thank Andy Göhrs, Eduard Höschele and the CONFET for assistance in the lab and helpful discussions.

References

[1]Bartlett, M. A. and Westermark, M. O., "A Study of Humidified Gas Turbines for Short-Term Realization in Midsized Power GenerationPart I: Nonintercooled Cycle Analysis," *Journal of Engineering for Gas Turbines and Power*, Vol. 127, No. 1, 2005, pp. 91.

[2]Bartlett, M. A. and Westermark, M. O., "A Study of Humidified Gas Turbines for Short-Term Realization in Midsized Power GenerationPart II: Intercooled Cycle Analysis and Final Economic Evaluation," *Journal of Engineering for Gas Turbines and Power*, Vol. 127, No. 1, 2005, pp. 100–108.

[3]Jonsson, M. and Yan, J., "Humidified gas turbinesa review of proposed and implemented cycles," *Energy*, Vol. 30, No. 7, June 2005, pp. 1013–1078.

[4]Bhargava, A., Colket, M., Sowa, W. A., Casleton, K., and Maloney, D., "An Experimental and Modeling Study of Humid Air Premixed Flames," *Journal of Engineering for Gas Turbines and Power*, Vol. 122, No. 3, 2000, pp. 405.

[5]Göke, S., Göckeler, K., Krüger, O., and Paschereit, C. O., "Computational and Experimental Study of Premixed Combustion at Ultra Wet Conditions," *Proceedings of GT2010 ASME Turbo Expo 2010: Power for Land, Sea and Air June 14-18, 2010, Glasgow, Scotland*, ASME Paper, GT2010-23417, 2010.

[6]Göke, S., Terhaar, S., Schimek, S., Göckeler, K., and Paschereit, C. O., "Combustion of Natural Gas, Hydrogen and Bio-Fuels at Ultra-Wet Conditions," *Proceedings of GT2011 ASME Turbo Expo 2011: Power for Land, Sea and Air June 6-10, 2011, Vancouver, Canada*, ASME Paper, GT2011-45696, 2011.

[7]Syred, N. and Beér, J., "Combustion in swirling flows: A review," *Combustion and Flame*, Vol. 23, No. 2, 1974, pp. 143–201.

[8]Clarke, A., Gerrard, A., and Holliday, L., "Some experiences in gas turbine combustion chamber practice using water flow visualization techniques," *Symposium (International) on Combustion*, Vol. 9, No. 1, 1963, pp. 878–891.

[9]Chigier, N. A. and Dvorak, K., "Laser Anemometer Measurements in Flames with Swirl," *Fifteenth International Symposium on Combustion, Tokyo, 1974*, 1974.

[10]Fujii, S. and Eguchi, K., "Swirling jets with and without combustion," *AIAA Journal*, 1981, pp. 1438–1442.

[11]Wicksall, D., Agrawal, A., Keller, J., and Schefer, R., "Influence of Hydrogen Addition on Flow Structure in Confined Swirling Methane Flame," *Journal of Propulsion and Power*, Vol. 21, No. 1, Jan. 2005, pp. 16–24.

[12]Vanoverberghe, K. P., Van Den Bulck, E. V., and Tummers, M. J., "Confined annular swirling jet combustion," *Combustion Science and Technology*, Vol. 175, No. 3, 2003, pp. 545–578.

[13]Durox, D., Schuller, T., Noiray, N., and Candel, S., "Experimental analysis of nonlinear flame transfer functions for different flame geometries," *Proceedings of the Combustion Institute*, Vol. 32, No. 1, 2009, pp. 1391–1398.

[14]Mazas, A., Fiorina, B., Lacoste, D., and Schuller, T., "Effects of water vapor addition on the laminar burning velocity of oxygen-enriched methane flames," *Accepted at Combustion and Flame*, 2011.

[15]Krüger, O., Göckeler, K., Göke, S., and Paschereit, C. O., "Numerical Investigations of a Swirl-Stabilized Premixed Flame at Ultra-Wet Conditions," *Proceedings of GT2011 ASME Turbo Expo 2011: Power for Land, Sea and Air June 6-10, 2011, Vancouver, Canada*, ASME Paper, GT2011-45866, 2011.

[16]Gu, X., Zang, S. S., and Ge, B., "Effect on flow field characteristics in methaneair non-premixed flame with steam addition," *Experiments in Fluids*, Vol. 41, No. 5, Sept. 2006, pp. 829–837.

[17]Göckeler, K., Göke, S., Schimek, S., and Paschereit, C. O., "Enhanced Recirculation in the Cold Flow Field of a Swirl-stabilized Burner for Ultra Wet Combustion," *Int. Conf. on Jets, Wakes and Separated Flows, ICJWSF September 27-30, 2010, Cincinnati, Ohio USA*, 2010.

[18]Oberleithner, K., Sieber, M., Nayeri, C. N., Paschereit, C. O., Petz, C., Hege, H.-C., Noack, B. R., and Wygnanski, I., "Three-dimensional coherent structures in a swirling jet undergoing vortex breakdown: stability analysis and empirical mode construction," *Journal of Fluid Mechanics*, 2011.

[19]Strangfeld, C., Göckeler, K., Terhaar, S., and Paschereit, C. O., "3D Visualisation of Measured Coherent Structures in a Swirling Water Flow," *Lasermethoden in der Strömungsmesstechnik, 6.-8. September 2011, Ilmenau, Germany, (Accepted)*, 2011.

[20]Escudier, M. P. and Keller, J., "Recirculation in swirling flow - A manifestation of vortex breakdown," *AIAA Journal*, Vol. 23, No. 1, Jan. 1985, pp. 111–116.

[21]Syred, N., "A review of oscillation mechanisms and the role of the precessing vortex core (PVC) in swirl combustion systems," *Progress in Energy and Combustion Science*, Vol. 32, No. 2, 2006, pp. 93–161.